Numerical Upscaling in Applied Geophysics. The Mesoscale

School of Earth Sciences and Engineering, Hohai University, Nanjing, China.

Juan E. Santos,

Universidad de Buenos Aires (UBA), Instituto del Gas y del Petróleo (IGPUBA), Argentina, and Department of Mathematics, Purdue University, West Lafayette, Indiana, USA.
Collaborators: J. M. Carcione (OGS), G. B. Savioli (IGPUBA) and P. M. Gauzellino, Universidad Nacional de La Plata

May 15, 2019

Seismic Waves in Hydrocarbon Reservoir Formations. I

- Hydrocarbon Reservoir Formations are fluid-saturated poroelastic media.
- Seimic waves generated near the earth surface or inside wells are used to detect and characterize these formations.
- M. Biot (1956, 1975,1962), presented a theory to describe the propagation of waves in a poroelastic medium saturated by a single-phase fluid (a Single Phase Biot medium, SPBM).
- Biot's theory predics the existence of two compressional waves (one fast (P1) and one slow (P2) and one shear (fast S) wave.

Seismic Waves in Hydrocarbon Reservoir Formations. II

- P1 or S-waves travelling through a SPBM containing heterogeneities at the mesoscopic scale suffer attenuation and dispersion observed in seismic data (mesoscopic loss).
- The mesoscopic-scale length is intended to be larger than the grain sizes but much smaller than the wavelength of the pulse.
- The mesoscopic loss effect occurs because different regions of the medium may undergo different strains and fluid pressures.
- This in turn induces fluid flow and Biot slow waves (WIFF) causing energy losses and velocity dispersion due to energy transfer between wave modes.

Numerical simulations illustrating the mesoscopic loss mechanism.

- The computational domain is a square of side length 800 m representing a SPBM alternately saturated with gas and water.
- The perturbation is a compressional point source applied to the matrix, located inside the region at $(x_s, y_s) = (400$ m, 4 m$)$ with (dominant) frequency 20 Hz.
- Biot's equations of motion were solved for 110 temporal frequencies in the interval $(0, 60Hz)$ employing a Finite Element (FE) parallelizable domain decomposition iterative procedure.
- The domain was discretized into square cells of side length $h = 40$ cm. The time domain solution was obtained performing an approximate inverse Fourier transform.

Time histories in a SPBM saturated by gas (top left), water (top right) and periodic gas-water (bottom)

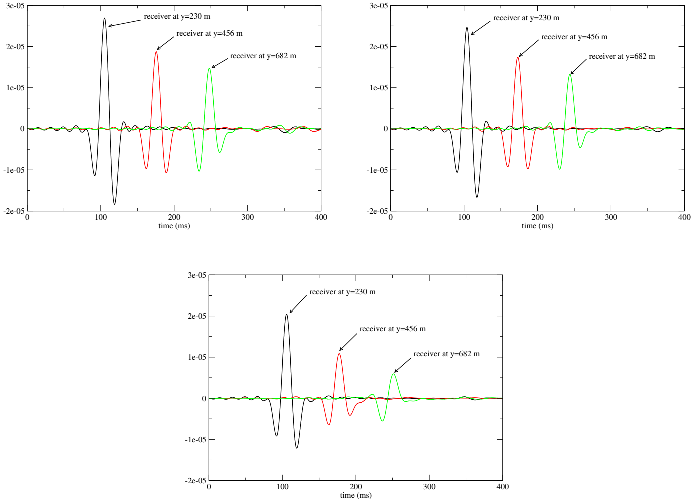

Time histories observed at a receiver in a SPBM saturated by gas, water and periodic gas-water.

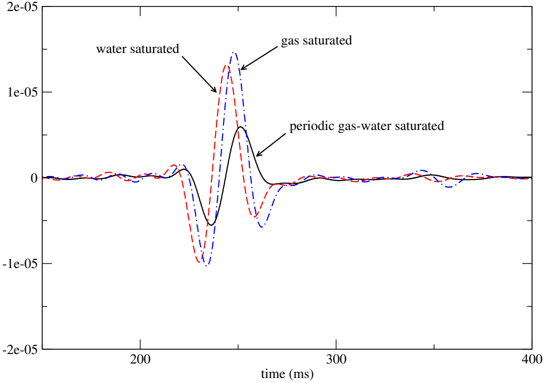

The delay in in the arrival time in the periodic gas-water case is due to the velocity dispersion caused by the mesoscopic scale heterogeneities. The associated attenuation was checked (by computing the numerical Q-factor) to be very good agreement with that predicted by White's theory.

Seismic Waves in Hydrocarbon Reservoir Formations. III

- Since extremely fine meshes are needed to represent mesoscopic-scale heterogeneities, numerical simulations using Biot's equations of motion are computationally expensive or not feasible.
- Alternative: In the context of Numerical Rock Physics, perform compressibility and shear time-harmonic experiments to determine an effective viscoelastic medium long-wave equivalent to a highly heterogeneous Biot medium.
- This effective viscoelastic medium, defined by a plane wave modulus $\overline{E}_u(\omega)$ and a shear modulus $\overline{G}_u(\omega)$, has in the average the same attenuation and velocity dispersion than the highly heterogeneous Biot medium.

Seismic Waves in Hydrocarbon Reservoir Formations. IV

- Each experiment is associated with a Boundary Value Problem (BVP) that is solved using the Finite Element Method (FEM).
- Numerical Rock Physics may, in many circumstances, offer an alternative to laboratory measurements. Numerical experiments are inexpensive and informative since the physical process of wave propagation can be inspected during the experiment.
- Moreover, they are repeatable, essentially free from experimental errors, and may easily be run using alternative models of the rock and fluid properties

Biot's model (SPBM) in the diffusive range of frequencies.

Frequency-domain stress-strain relations in a Biot medium saturated by a single-phase fluid:

$$\tau_{kl}(\mathbf{u}) = 2G\,\epsilon_{kl}(\mathbf{u}^s) + \delta_{kl}\left(\lambda_u \nabla\cdot\mathbf{u}^s + B\nabla\cdot\mathbf{u}^f\right),$$
$$p_f(\mathbf{u}) = -B\nabla\cdot\mathbf{u}^s - M\nabla\cdot\mathbf{u}^f,$$

$\mathbf{u} = (\mathbf{u}^s, \mathbf{u}^f)$, $\mathbf{u}^s = (u_1^s, u_3^s), \mathbf{u}^f = (u_1^f, u_3^f)$.

Biot's equations in the diffusive range:

$$\nabla\cdot\tau(\mathbf{u}) = 0,$$
$$\mathrm{i}\omega\mu\kappa^{-1}\mathbf{u}^f + \nabla p_f(\mathbf{u}) = 0,$$

μ: fluid viscosity, κ:frame permeability.

Biot's equations are solved in the 2-D case on a square sample $\Omega = (0, L)^2$ with boundary $\Gamma = \Gamma^L \cup \Gamma^B \cup \Gamma^R \cup \Gamma^T$ in the (x_1, x_3)-plane. The domain Ω is a representative sample of our fluid saturated poroelastic material.

$$\Gamma^L = \{(x_1, x_3) \in \Gamma : x_1 = 0\}, \quad \Gamma^R = \{(x_1, x_3) \in \Gamma : x_1 = L\},$$
$$\Gamma^B = \{(x_1, x_3) \in \Gamma : x_3 = 0\}, \quad \Gamma^T = \{(x_1, x_3) \in \Gamma : x_3 = L\}.$$

For determining the complex plane wave modulus $\overline{E}_u(\omega)$, solve Biot's equations with the boundary conditions

$$\tau(\mathbf{u})\nu \cdot \nu = -\Delta P, \quad (x_1, x_3) \in \Gamma^T,$$
$$\tau(\mathbf{u})\nu \cdot \chi = 0, \quad (x_1, x_3) \in \Gamma,$$
$$\mathbf{u}^s \cdot \nu = 0, \quad (x_1, x_3) \in \Gamma \setminus \Gamma^T,$$
$$\mathbf{u}^f \cdot \nu = 0, \quad (x_1, x_3) \in \Gamma.$$

The complex P-wave modulus of a viscoelastic medium long-wave equivalent to an heterogeneous Biot medium. II

The *equivalent* undrained complex plane-wave modulus $\overline{E_u}(\omega)$ is determined by the relation

$$\frac{\Delta V(\omega)}{V} = -\frac{\Delta P}{\overline{E_u}(\omega)},$$

V: original volume of the sample.
Then to approximate $\Delta V(\omega)$ use

$$\Delta V(\omega) \approx L u_3^{s,T}(\omega).$$

$u_3^{s,T}(\omega)$: average vertical solid displacements $u_3^s(x_1, L, \omega)$ on Γ^T.

For determining the complex shear modulus $\overline{G}_u(\omega)$, solve Biot's equations with the boundary conditions

$$-\tau(\mathbf{u})\nu = \mathbf{g}, \quad (x_1, x_3) \in \Gamma^T \cup \Gamma^L \cup \Gamma^R,$$
$$\mathbf{u}^s = 0, \quad (x, y) \in \Gamma^B,$$
$$\mathbf{u}^f \cdot \nu = 0, \quad (x, y) \in \Gamma,$$

$$\mathbf{g} = \begin{cases} (0, \Delta T), & (x_1, x_3) \in \Gamma^L, \\ (0, -\Delta T), & (x_1, x_3) \in \Gamma^R, \\ (-\Delta T, 0), & (x_1, x_3) \in \Gamma^T. \end{cases}$$

The change in shape of the rock sample allows to recover its *equivalent* complex shear modulus $\overline{G}_u(\omega)$ using the relation

$$\mathrm{tg}(\theta(\omega)) = \frac{\Delta T}{\overline{G}_u(\omega)},$$

$\theta(\omega)$: departure angle from the original positions of the lateral boundaries

The complex shear modulus of a viscoelastic medium long-wave equivalent to an heterogenous Biot medium. II

To find an approximation to $\mathrm{tg}(\theta(\omega))$, compute the average horizontal displacement $u_1^{s,T}(\omega)$ of the horizontal displacements $u_1^s(x_1, L, \omega)$ at the top boundary Γ^T. Then use

$$\mathrm{tg}(\theta(\omega)) \approx u_1^{s,T}(\omega)/L,$$

to determine the shear modulus $\overline{G}_u(\omega)$

Schematic representation of the experiments to determine the complex P-wave and shear modulus

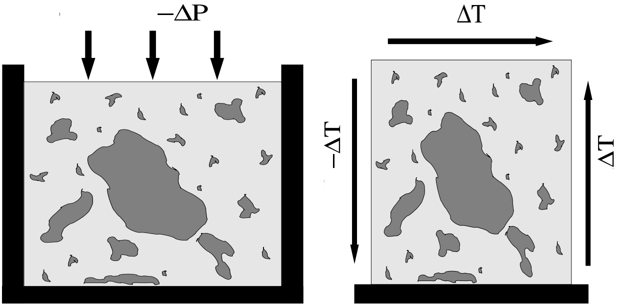

Figures (a) show how to determine $\overline{E}_u(\omega)$, (b) show how to determine $\overline{G}_u(\omega)$.

Solution of the BVP's using the Finite Element (FE) Method.

The mesh size h of the Finte Element spatial discretization has to be small enough so that diffusion process associated with the fluid pressure equilibration is accurately resolved. The diffusion length is given by the relation length

$$L_d = \sqrt{\frac{2\pi\kappa K_f}{\mu\omega}}, \quad K_f = \text{fluid bulk modulus}$$

We take h so that the minimum diffusion length is discretized with at least 3 mesh points at the highest frequency, which is sufficient to represent a (smooth) diffusion-type process. Besides, the size of the rock sample is not arbitrary: it has to be big enough to constitute a representative part of the Biot medium but, at the same time, it has to be much smaller than the wavelengths associated with each frequency.

Solution of the BVP's using the FE method. Local DOF.

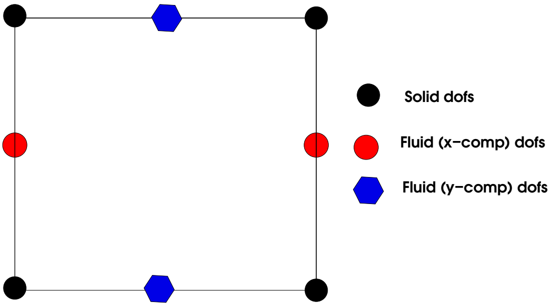

The solution of the time-harmonic tests was computed using the FEM. The figure displays the local degrees of freedom (DOFs) associated with each component of the solid displacement and the fluid displacement vectors. Once we computed the p_{IJ} coefficients, we can determine the velocities and dissipation factors of the equivalent TIV medium.

Determination of $\overline{E}_u(\omega)$ in patchy gas-brine saturated rocks.

Patchy gas-brine saturation arises in hydrocarbon reservoirs, where regions of non-uniform patchy saturation occur at gas-brine contacts. Patchy-saturation patterns produce very important mesoscopic loss effects at the seismic band of frequencies, as was first shown by J. E. White (GPY, 1975).

To study these effects, consider porous samples with spatially variable gas-brine distribution in the form of irregular patches fully saturated with gas and zones fully saturated with brine. The domain Ω is a square of side length 50 cm, and a 75×75 mesh uniform is used.

Patchy gas-brine distribution for two different correlation lengths. White zones: full gas saturation, black zones: full brine saturation

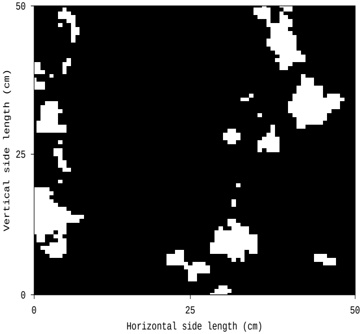

(a)

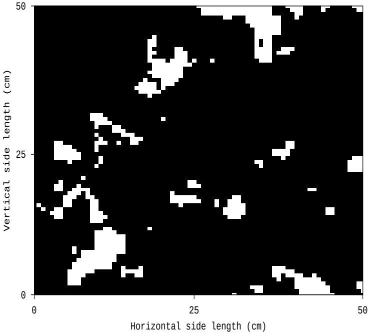

(b)

(a): correlation length 10 cm (b): correlation lengths 5 cm.

Compressional phase velocity and inverse quality factors for two different correlation lengths CL

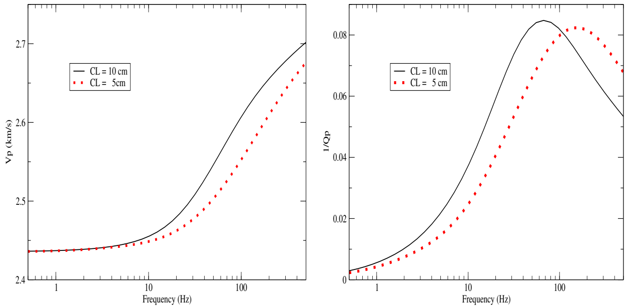

(a) (b)

(a): Compressional phase velocity (b): Inverse quality factors. Notice the attenuation peak moving to higher frequencies for the shorter CL.

Pressure distribution (Pa) at two different frequencies.

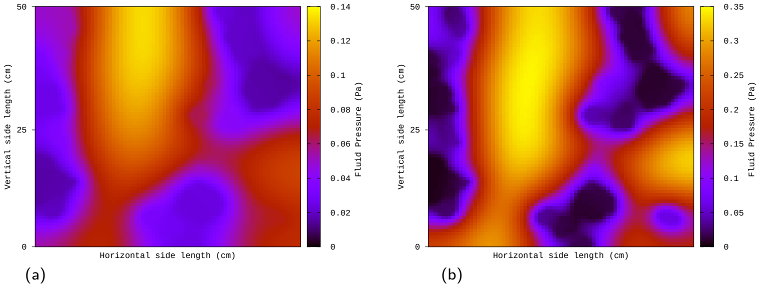

(a): 10 Hz (b): 60 Hz.

Gradient of pressures can be seen at the gas-water interfaces, stronger at 65 Hz than at 10 Hz. This Figure illustrates the mesoscopic loss mechanism.

The effective shear modulus when the solid matrix is composed of two different materials.

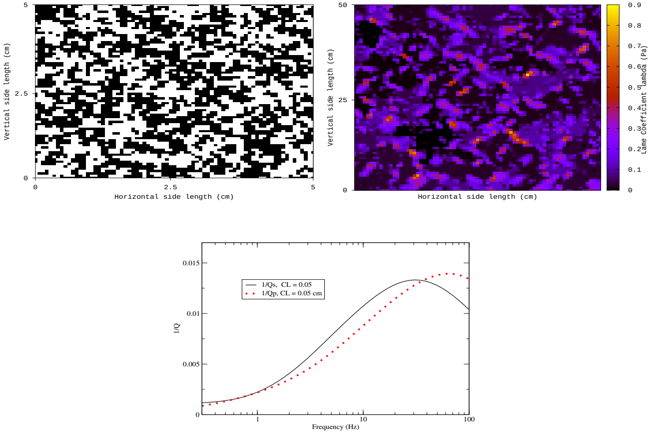

Top left: Fractal shale-sandstone distribution. Black zones correspond to pure shale and white ones to pure sandstone. Shale percentage is 50 %. Top right: Absolute fluid pressure distribution (Pa) at 30 Hz. Bottom: Inverse quality factors Q_s and Q_p. Q_s of about 75 between 20 and 40 Hz, Q_p about 70 at 65 Hz. Conclusion: wave induced fluid flow (mesoscopic loss) is observed when shear and compressional waves propagate through Biot media with highly heterogeneous solid frames.

Waves in porous rocks saturated by two-phase fluids. I

- For two-phase fluids, the SPBM does not take into account capillary forces and interference between the two fluids as they flow within the pore space.
- Those effects are taken into account when using a theory for the case of a poroelastic medium saturated by a two-phase fluid (a two-phase Biot medium - 2PBM) (Santos et al., 1990a, 1990b, Ravazzoli et al., 2003).
- The theory predicts the existence of one fast (P1) and two slow (P2, P3) compressional waves and one shear (S) wave.
- Capillary forces are responsible for the existence of one additional slow wave, while relative permeability functions model energy losses due to interferences between the two fluids as they flow, modifying the WIFF mechanism.

Anisotropy in shale reservoir rocks. I

- Most shale reservoir rocks are laminated media of very low permeability composed of illite-smectite layers and organic matter in the form of oil, gas and kerogen.
- For seismic wavelengths much larger than the thickness of the layers, these laminated materials behave as homogeneous viscoelastic transversely isotropic (VTI) media.
- Here we define a set of five harmonic experiments to determine the stiffness coefficients of a long-wave equivalent VTI medium to a densely fractured 2PBM.
- The experiments are formulated as boundary value problems (BVP) in the space-frequency domain that are solved using the finite element (FE) method.

Anisotropy in shale reservoir rocks. II

- This VTI medium has, in the average, the same attenuation and velocity dispersion than the highly heterogeneous Biot medium.
- Each experiment is associated with a Boundary Value Problem (BVP) that is solved using the Finite Element Method (FEM).
- A detailed explanation on these experiments and the FE method can be found in **Numerical Simulation in Applied Geophysics, Springer, 2017**.

The model describing a poroelastic medium saturated by a two-phase fluid (2PBM). I

In a 2PBM we have *wetting* and *non-wetting* fluid phases, denoted with the subscripts (or superscripts) "w" and "n", respectively, while "s" indicates the solid phase.

S_l, S_{rl}: saturation and residual saturation of the l-phase, $l = n, w$, so that $S_{rn} < S_n < 1 - S_{rw}$.

Assuming fully saturation of the pore space, $S_w + S_n = 1$
The relative particle fluid displacements are

$$\mathbf{u}^{\ell} = \phi(\tilde{\mathbf{u}}^{\ell} - \mathbf{u}^{s}),\ \xi^{\ell} = -\nabla \cdot \mathbf{u}^{\ell},\ \ell = n, w.$$

where $\mathbf{u}^s = (u_i^s)$, $\tilde{\mathbf{u}}^l = (\tilde{u}_i^l)$ $\ell = n, w,\ i = 1, 2, 3$ are the time Fourier transforms of the displacement vectors of the solid and fluid phases and ϕ is the matrix effective porosity.

The model describing a poroelastic medium saturated by a two-phase fluid (2PBM). II

$\tau = \tau_{ij}$, $\varepsilon = \varepsilon_{ij}$, $i, j = 1, 2, 3$: time Fourier transforms of the stress and strain tensors, respectively,

P_l: time Fourier transform of the infinitesimal change in the pressure of the l-fluid phase, taken with respect to the reference value $\bar{P}_l$ $l = n, w$.

This reference value is associated with the initial equilibrium state having non-wetting fluid saturation $\bar{S}_n$ and porosity $\bar{\phi}$.

Capillary relation

$$P_{ca} = P_{ca}(S_n + \bar{S}_n) = \bar{P}_n + P_n - (\bar{P}_w + P_w) = P_{ca}(\bar{S}_n) + P_n - P_w \geq 0. \tag{1}$$

The model describing a poroelastic medium saturated by a two-phase fluid (2PBM). III

The stress-strain relations in a 2PBM are (Santos et al., 1990a, Ravazzoli et al. 2003):

$$
\begin{aligned}
\tau_{ij}(\mathbf{u}) &= 2N\,\varepsilon_{ij} + \delta_{ij}(\lambda_u\, e^s - B_1\,\xi^n - B_2\,\xi^w),\\
\mathcal{T}_n(\mathbf{u}) &= \left(\bar{S}_n + \beta + \zeta\right) P_n - (\beta + \zeta)\, P_w\\
&= -B_1\, e^s + M_1\,\xi^n + M_3\,\xi^w,\\
\mathcal{T}_w(\mathbf{u}) &= \left(\bar{S}_w + \zeta\right)\, P_w - \zeta\, P_n = -B_2\, e^s + M_3\,\xi^n + M_2\,\xi^w,
\end{aligned}
$$

$$
\beta = \frac{P_{ca}(\overline{S}_n)}{P'_{ca}(\bar{S}_n)}, \quad \zeta = \frac{\overline{P_w}}{P'_{ca}(\bar{S}_n)}.
$$

τ, $\mathcal{T}_n$, $\mathcal{T}_w$: generalized forces in a 2PBM.

The model describing a poroelastic medium saturated by a two-phase fluid (2PBM). IV

The diffusive equations for a 2PBM:

$$\frac{\partial \tau_{ij}}{\partial x_j} = 0,$$

$$i\omega\,(\bar{S}_n)^2 \frac{\eta_n}{\kappa K_{rn}(\bar{S}_n)}\, u_j^n - i\omega\, d_{nw}\, u_j^w + \frac{\partial \mathcal{T}_n}{\partial x_j} = 0,$$

$$i\omega\,(\bar{S}_w)^2 \frac{\eta_w}{\kappa K_{rw}(\bar{S}_w)}\, u_j^w - i\omega\, d_{nw}\, u_j^n + \frac{\partial \mathcal{T}_w}{\partial x_j} = 0, \quad j = 1,2,3$$

$$d_{nw}(\bar{S}_n, \bar{S}_w) = \epsilon \left((\bar{S}_n)^2 \frac{\eta_n}{\kappa K_{rn}(\bar{S}_n)} \right) \left((\bar{S}_w)^2 \frac{\eta_w}{\kappa K_{rw}(\bar{S}_w)} \right).$$

η_n, η_w; fluid viscosities
κ, $K_{rn}(S_n), K_{rw}(S_w)$; the absolute and relative permeabilities.

The model describing a poroelastic medium saturated by a two-phase fluid (2PBM). IV

Choice of relative permeability and capillary pressure functions:

$$K_{rn}(S_n) = (1 - (1 - S_n)/(1 - S_{rn}))^2 \,,$$
$$K_{rw}(S_n) = ([1 - S_n - S_{rw}] \,/\, (1 - S_{rw}))^2 \,,$$
$$P_{ca}(S_n) = A \left(1/(S_n + S_{rw} - 1)^2 - S_{rn}^2/[S_n(1 - S_{rn} - S_{rw})]^2 \right.$$

A: Capillary pressure amplitude, chosen to be 30 kPa.

Remarks on effective and relative permeability functions.

Reservoirs contain up to three phases: oil, water and gas and each phase interferes with the flow of the others.
The permeability of a reservoir rock to any one fluid j in the presence of others is its effective permeability κ_j, which depends on saturation. It is defined through a generalization of Darcy's Law:

$$\frac{Q_j}{A} = -\frac{\kappa_j}{\mu_j}\frac{\partial p_j}{\partial x}, \qquad j = o, g, w$$

where Q_j is the flow rate, A the cross sectional area to flow, μ_j the fluid viscosity and p_j the fluid pressure.
Relative permeability κ_{rj} to any one fluid j is the ratio of effective permeability κ_j to absolute permeability κ.
Therefore, Darcy's Law becomes:

$$\frac{Q_j}{A} = -\frac{\kappa\kappa_{rj}}{\mu_j}\frac{\partial p_j}{\partial x}$$

Relative permeability can be expressed as a number between 0 and 1.0 or as a percent. Pore type and formation wettability affect relative permeability.

Capillary pressure and relative permeability functions.

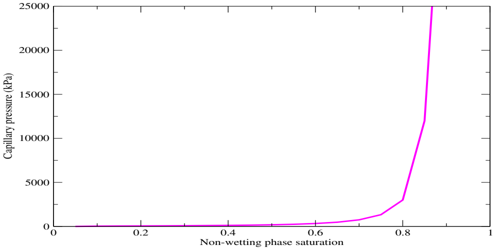

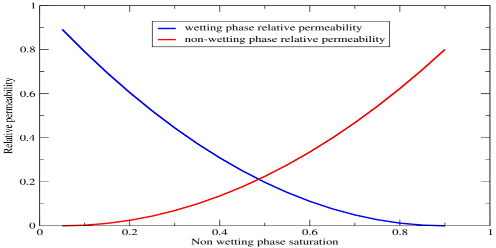

The equivalent VTI medium. I

A 2PBM with a set of horizontal layers behaves as a VTI medium with vertical (x_3) symmetry axis at long wavelengths
$\sigma_{ij}(\widetilde{\mathbf{u}}_s)$, $e_{ij}(\widetilde{\mathbf{u}}_s)$: stress and strain tensor components of the VTI medium,
$\widetilde{\mathbf{u}}_s$: solid displacement vector at the macroscale.
The stress-strain relations assuming a closed system:

$$
\begin{aligned}
\sigma_{11}(\widetilde{\mathbf{u}}_s) &= p_{11}\ e_{11}(\widetilde{\mathbf{u}}_s) + p_{12}\ e_{22}(\widetilde{\mathbf{u}}_s) + p_{13}\ e_{33}(\widetilde{\mathbf{u}}_s),\\
\sigma_{22}(\widetilde{\mathbf{u}}_s) &= p_{12}\ e_{11}(\widetilde{\mathbf{u}}_s) + p_{11}\ e_{22}(\widetilde{\mathbf{u}}_s) + p_{13}\ e_{33}(\widetilde{\mathbf{u}}_s),\\
\sigma_{33}(\widetilde{\mathbf{u}}_s) &= p_{13}\ e_{11}(\widetilde{\mathbf{u}}_s) + p_{13}\ e_{22}(\widetilde{\mathbf{u}}_s) + p_{33}\ e_{33}(\widetilde{\mathbf{u}}_s),\\
\sigma_{23}(\widetilde{\mathbf{u}}_s) &= 2\ p_{55}\ e_{23}(\widetilde{\mathbf{u}}_s),\\
\sigma_{13}(\widetilde{\mathbf{u}}_s) &= 2\ p_{55}\ e_{13}(\widetilde{\mathbf{u}}_s),\\
\sigma_{12}(\widetilde{\mathbf{u}}_s) &= 2\ p_{66}\ e_{12}(\widetilde{\mathbf{u}}_s).
\end{aligned}
$$

Note that in a VTI medium $p_{12} = p_{11} - 2p_{66}$,

The equivalent VTI medium. II

The stiffness p_{IJ} can be determined using five time-harmonic experiments.
x_1 and x_3: horizontal and vertical coordinates'
We solve the diffusive equations equations in the 2D case on a reference square $= (0, L)^2$ with boundary Γ in the (x_1, x_3)-plane. Set $\Gamma = \Gamma^L \cup \Gamma^B \cup \Gamma^R \cup \Gamma^T$, where $\Gamma^L, \Gamma^R, \Gamma^B$ and Γ^T denote the left, right, bottom and top boundaries of .
$\{\nu, \ \chi\}$ the unit outer normal and a unit tangent oriented counterclockwise on Γ
To determine the five p_{IJ} stiffness coefficients, we solve he diffusive equations in with the boundary conditions

$$\mathbf{u}^n \cdot \nu = 0, \quad \mathbf{u}^w \cdot \nu = (x_1, x_3) \in \Gamma,$$

i.e., no fluids enter or leave the sample, and the following additional boundary conditions.

The equivalent VTI medium, experiment to determine p_{33}.

$$\tau(\mathbf{u})\nu \cdot \nu = -\Delta P, \quad (x_1, x_3) \in \Gamma^T,$$
$$\tau(\mathbf{u})\nu \cdot \chi = 0, \quad (x_1, x_3) \in \Gamma,$$
$$\mathbf{u}^s \cdot \nu = 0, \quad (x_1, x_3) \in \Gamma \setminus \Gamma^T.$$

Using the relation

$$\frac{\Delta V(\omega)}{V} = -\frac{\Delta P}{p_{33}(\omega)}, \tag{2}$$

where V is the original volume of the sample, $p_{33}(\omega)$ can be determined from equation (2) measuring the complex volume change $\Delta V(\omega) \approx L u_{s,3}^{(33,T)}(\omega)$, where $u_{s,3}^{(33,T)}()$ is the average of the vertical component of the solid phase at the boundary Γ^T.

The equivalent VTI medium, experiment to determine p_{11}

$$
\begin{aligned}
&\tau(\mathbf{u})\nu \cdot \nu = -\Delta P, \quad (x_1, x_3) \in \Gamma^R, \\
&\tau(\mathbf{u})\nu \cdot \chi = 0, \quad (x_1, x_3) \in \Gamma, \\
&\mathbf{u}^s \cdot \nu = 0, \quad (x_1, x_3) \in \Gamma \setminus \Gamma^R.
\end{aligned}
$$

Thus, this experiment determines p_{11} as indicated for p_{33}, measuring the oscillatory volume change.

The equivalent VTI medium, experiment to determine p_{13}

$$\tau(\mathbf{u})\nu \cdot \nu = -\Delta P, \quad (x_1, x_3) \in \Gamma^R \cup \Gamma^T,$$
$$\tau(\mathbf{u})\nu \cdot \chi = 0, \quad (x_1, x_3) \in \Gamma,$$
$$\mathbf{u}^s \cdot \nu = 0, \quad (x_1, x_3) \in \Gamma^L \cup \Gamma^B.$$

From the first and third macroscopic constitutive relations we get

$$\sigma_{11} = p_{11}\epsilon_{11} + p_{13}\epsilon_{33} \quad \sigma_{33} = p_{13}\epsilon_{11} + p_{33}\epsilon_{33},$$

with ϵ_{11} and ϵ_{33} being the (macroscale) strain components at Γ^L and Γ^T, respectively. Since $\sigma_{11} = \sigma_{33} = -\Delta P$ we obtain $p_{13}()$ as

$$p_{13}(\omega) = \frac{p_{11}\epsilon_{11} - p_{33}\epsilon_{33}}{\epsilon_{11} - \epsilon_{33}}.$$

The equivalent VTI medium, experiment to determine p_{55}

$$-\tau(\mathbf{u})\nu = \mathbf{g}, \quad (x_1, x_3) \in \Gamma^T \cup \Gamma^L \cup \Gamma^R,$$
$$\mathbf{u}_s = 0, \quad (x_1, x_3) \in \Gamma^B,$$

$$\mathbf{g} = \begin{cases} (0, \Delta G), & (x_1, x_3) \in \Gamma^L, \\ (0, -\Delta G), & (x_1, x_3) \in \Gamma^R, \\ (-\Delta G, 0), & (x_1, x_3) \in \Gamma^T. \end{cases}$$

The change in shape of the sample allows to obtain $p_{55}(\omega)$ by using the relation

$$\mathrm{tg}(\beta\omega) = \frac{\Delta G}{p_{55}(\omega)},$$

$\beta(\omega)$: the departure angle between the original positions of the lateral boundaries and those after applying the shear stresses, that can be determined by measuring the average horizontal displacement at Γ^T.

The equivalent VTI medium, experiment to determine p_{66}

$$-\tau(\mathbf{u})\nu = \mathbf{g}_2, \quad (x_1, x_2) \in \Gamma^B \cup \Gamma^R \cup \Gamma^T,$$
$$\mathbf{u}_s = 0, \quad (x_1, x_2) \in \Gamma^L,$$

$$\mathbf{g}_2 = \begin{cases} (\Delta G, 0), & (x_1, x_2) \in \Gamma^B, \\ (-\Delta G, 0), & (x_1, x_2) \in \Gamma^T, \\ (0, -\Delta G), & (x_1, x_2) \in \Gamma^R. \end{cases}$$

Then, we proceed as indicated for $p_{55}(\omega)$.

Illustration of the five time-harmonic experiments to determine the stiffness coefficients.

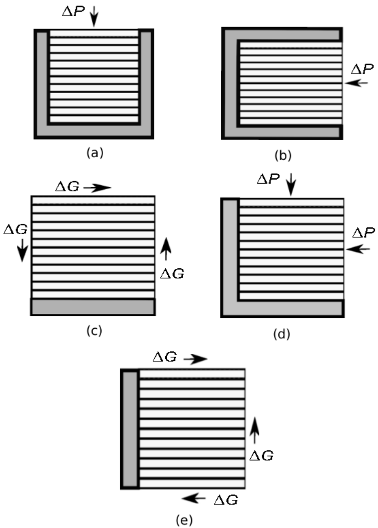

Figures 1(a) and 1(b) show how to compute p_{33} and p_{11}, while Figures 1(c) and 1(e) display the experiments determining p_{55} and p_{66}. Figure 1(d) illustrates the experiment to determine p_{13}.

Velocities and attenuation in VTI media. I

Complex velocities of the equivalent VTI anisotropic medium:

$$
\begin{aligned}
v_{\mathrm{qP}} &= (2\bar{\rho})^{-1/2}\sqrt{p_{11} l_1^2 + p_{33} l_3^2 + p_{55} + A},\\
v_{\mathrm{qSV}} &= (2\bar{\rho})^{-1/2}\sqrt{p_{11} l_1^2 + p_{33} l_3^2 + p_{55} - A},\\
v_{\mathrm{SH}} &= \bar{\rho}^{-1/2}\sqrt{p_{66} l_1^2 + p_{55} l_3^2},
\end{aligned}
$$

$$
A = \sqrt{[(p_{11} - p_{55}) l_1^2 + (p_{55} - p_{33}) l_3^2]^2 + 4[(p_{13} + p_{55}) l_1 l_3]^2}.
$$

$\bar{\rho} = \langle \rho \rangle$: average bulk density,

$l_1 = \sin\theta$, $l_3 = \cos\theta$ are the directions cosines, θ is the propagation angle between the wavenumber vector and the x_3-symmetry axis and the three velocities correspond to the qP, qS and SH waves, respectively.

Velocities and attenuation in VTI media. II

The seismic phase velocity and quality factors are:

$$v_p = \left[\mathrm{Re}\left(\frac{1}{v}\right)\right]^{-1} \quad \text{and} \quad Q = \frac{\mathrm{Re}(v^2)}{\mathrm{Im}(v^2)},$$

where v represents either v_{qP}, v_{qSV} or v_{SH}.

The energy-velocity vector $\mathbf{v}_e$ of the qP and qSV waves is

$$\frac{\mathbf{v}_e}{v_p} = (l_1 + l_3 \cot\psi)^{-1}\hat{\mathbf{e}}_1 + (l_1 \tan\psi + l_3)^{-1}\hat{\mathbf{e}}_3,$$

ψ: angle between the energy-velocity vector and the x_3-axis.

The energy velocity of the SH wave is

$$\mathbf{v}_e = \frac{1}{\bar{\rho} v_p}\left(l_1 p_{66}\hat{\mathbf{e}}_1 + l_3 p_{55}\hat{\mathbf{e}}_3\right).$$

Numerical Experiments. Anisotropy in source rocks

The FE experiments consider square periodic layered samples of side length 0.09 cm with 6 periods of illite-smectite and kerogen layers as in the Figure below

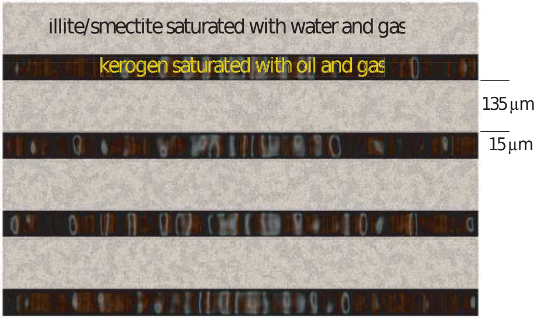

Schematic model of the Vaca Muerta formation.

Numerical Experiments. Anisotropy in source rocks

The FE experiments consider square periodic layered samples of side length 0.09 cm with 6 periods of illite-smectite and kerogen layers as in Figure 1 discretized by using a 60 $\times$ 60 uniform mesh. The material properties are given in Table 1.

Table 1. Material Properties.

Property	illite/smectite	kerogen	water	oil	gas
K_s (GPa)	28.4	7	2.25	0.57	0.022
K_m (GPa)	18	4.3	–	–	–
μ_m (GPa)	12.5	1.3	–	–	–
ρ_s (g/cm^3)	2.7	1.4	1	0.7	0.078
ϕ (%)	10	10	–	–	–
η (cP)	–	–	1	10	0.015
κ (ndarcy)	200	200	–	–	–
S_w(%)	99	0	–	–	–
S_o(%)	0	90	–	–	–
S_g(%)	1	10	–	–	–

Anisotropy in source rocks. Validation. I

We consider 6 periods of 0.0135 cm of illite-smectite and 0.0015 cm of kerogen layers, each layer saturated by a two-phase fluid.

In the illite-smectite layers, the wetting and non-wetting phases are water and gas, with residual saturations $S_{rw} = 4.5\,\%$ and $S_{rg} = 0$, respectively, and gas saturation is $S_g = 1\,\%$.

In the kerogen layers, the wetting and non-wetting phases are oil and gas, with residual saturations $S_{rw} = S_{ro} = 4.5\,\%$ and $S_{rg} = 0$, respectively, and gas saturation is $S_g = 10\,\%$.

The experiments compare energy velocities and dissipation factors of qP, qSV and SH waves computed

by using the 2PBM, when the sample is saturated by a two-phase fluid mixture, with the velocities

obtained with the analytical solution using the SPBM model as in Krzikalla and Müller (2011).

Anisotropy in source rocks. Validation. II

The effective single phase fluid viscosity $\eta^{(eff)}$, density $\rho^{(eff)}$ and bulk modulus $K^{(eff)}$ used in the SPBM were obtained as Reuss averages for the bulk moduli and arithmetic averages for densities and viscosities:

$$\eta^{(eff)} = \eta_n S_n + \eta_w S_w,$$
$$\rho^{(eff)} = \rho_n S_n + \rho_w S_w,$$
$$\frac{1}{K^{(eff)}} = \frac{S_n}{K_n} + \frac{S_w}{K_w}.$$

Energy velocities of qP and qSV waves at 50 Hz. Validation. III

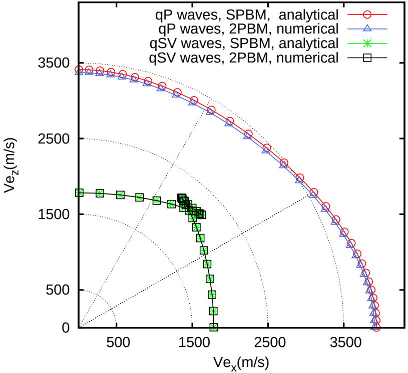

Polar representation of the energy velocities of qP and qSV waves for the FE 2PBM and analytical SPBM models at 50 Hz. The medium consists of a sequence of nine water-gas saturated illite-smectite layers and one oil-gas saturated kerogen layer (relation 9-1). The results of the analytical model were obtained using effective single-phase fluids.

Dissipation factors of qP waves at 50 Hz. Validation. IV

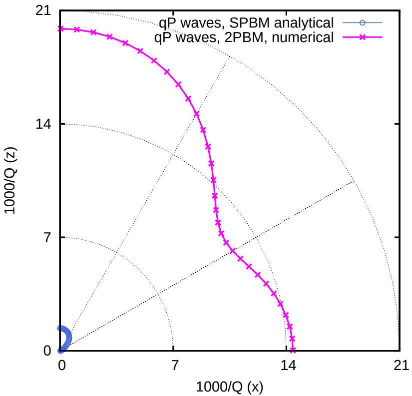

Polar representation of the dissipation factors of qP waves for the FE 2PBM and analytical SPBM models at 50 Hz. The medium consists of a sequence of nine water-gas saturated illite-smectite layers and one oil-gas saturated kerogen layer. The results of the analytical model were obtained using effective single-phase fluids.

Dissipation factors of qSV waves at 50 Hz. Validation. V

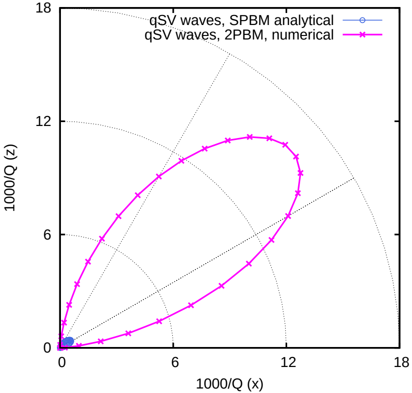

Polar representation of the dissipation factors of qSV waves for the FE 2PBM and analytical SPBM models at 50 Hz. The medium consists of a sequence of nine water-gas saturated illite-smectite layers and one oil-gas saturated kerogen layer. The results of the analytical model were obtained using effective single-phase fluids.

Energy velocities of SH waves at 50 Hz. Validation. VI

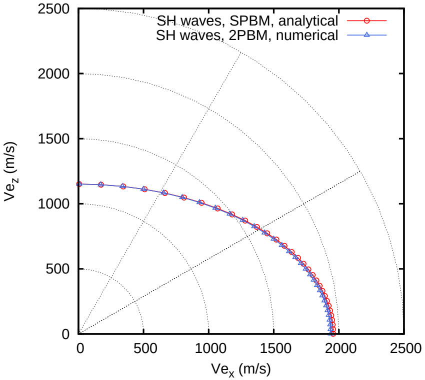

Polar representation of energy velocities of SH waves for the FE 2PBM and analytical SPBM models at 50 Hz. The medium consists of a sequence of nine water-gas saturated illite-smectite layers and one oil-gas saturated kerogen layer. The results of the analytical model were obtained using effective single-phase fluids.

Sensitivity to gas saturation in the kerogen layers. Dissipation factors of qP waves

Energy velocities of the qP and qSV waves for the 2PBM are not sensitive to changes in gas saturation in the kerogen layers, but dissipation factors exhibit strong differences as observed in the the two Figures below. Here and in what follows $S_{rg} = 0, S_{rw} = 10\,\%$. Relative permeabilities are responsible for the high attenuation predicted by the 2PBM model.

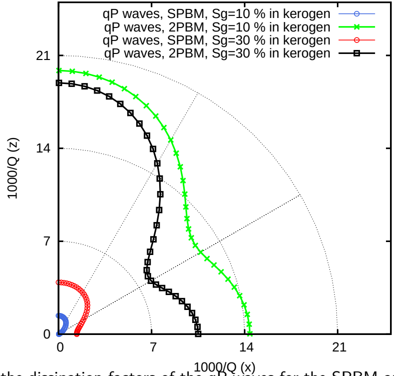

Polar representation of the dissipation factors of the qP waves for the SPBM and 2PBM models at 50 Hz as a function of gas saturation in kerogen layers. The medium consists of a sequence of nine water-gas saturated illite-smectite layers and one oil-gas saturated kerogen layer.

Sensitivity to gas saturation in kerogen layers. Dissipation factors of qSV waves.

Dissipation factors of qSV waves for the SPBM and 2PBM models at 50 Hz. $S_{rg} = 0$, $S_{rw} = 10\,\%$.

Relative permeabilities are responsible for the high attenuation predicted by the 2PBM model.

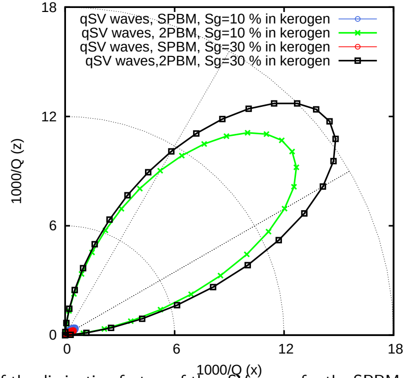

Polar representation of the dissipation factors of the qSV waves for the SPBM and 2PBM models at 50 Hz as a function of gas saturation in kerogen layers. The medium consists of a sequence of nine water-gas saturated illite-smectite layers and one oil-gas saturated kerogen layer.

Sensitivity to kerogen concentration. Energy velocities of qP waves

The sample is the same of the validation experiments but considering 6 periods of 0.012 cm of illite-smectite and 0.003 cm of kerogen (20 % kerogen) and 6 periods of 0.0105 cm of illite-smectite and 0.0045 cm of kerogen (30 % kerogen). $S_g = 10\,\%$ in the illite-smectite and kerogen layers.

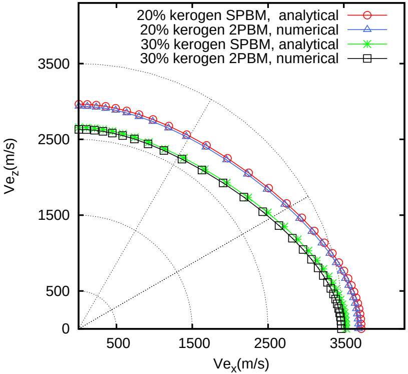

Polar representation of the energy velocities of the qP waves for the FE 2PBM and SPBM models at 50 Hz as a function of kerogen concentration. The medium consists of a sequence of eight (seven) water-gas saturated illite-smectite layers and two (three) oil-gas saturated kerogen layer. Lower velocity corresponds to higher kerogen content.

Sensitivity to kerogen concentration. Energy velocities of qSV waves

The sample is the same of the validation experiments but considering 6 periods of 0.012 cm of illite-smectite and 0.003 cm of kerogen (20 % kerogen) and 6 periods of 0.0105 cm of illite-smectite and 0.0045 cm of kerogen (30 % kerogen).$S_g = 10\,\%$ in the illite-smectite and kerogen layers.

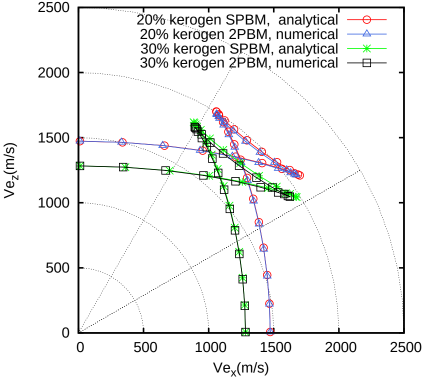

Polar representation of the energy velocities of qSV waves for the FE 2PBM and SPBM models at 50 Hz as a function of kerogen concentration. The medium consists of a sequence of eight (seven) water-gas saturated illite-smectite layers and two (three) oil-gas saturated kerogen layer. Lower velocity corresponds to higher kerogen content.

Sensitivity to kerogen concentration. Dissipation factors of qP waves

The sample is the same of the validation experiments but considering 6 periods of 0.012 cm of illite-smectite and 0.003 cm of kerogen (20 % kerogen) and 6 periods of 0.0105 cm of illite-smectite and 0.0045 cm of kerogen (30 % kerogen). $S_g = 10\,\%$ in the illite-smectite and kerogen layers.

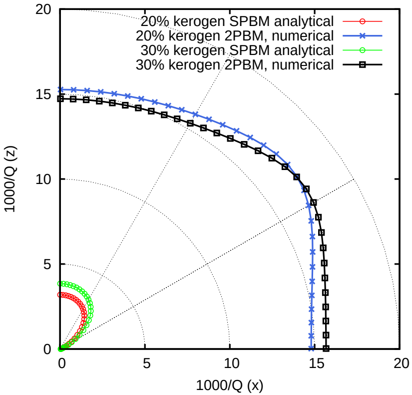

Polar representation of dissipation factors of qP waves for the FE 2PBM and SPBM models at 50 Hz as a function of kerogen concentration. The medium consists of a sequence of eight (seven) water-gas saturated illite-smectite layers and two (three) oil-gas saturated kerogen layer. Dissipation factors are much higher for the 2PBM model than for the SPBM model. These experiments indicate that the SPBM model is not reliable for predicting attenuation in multiphase saturated porous rocks.

Sensitivity to kerogen concentration. Dissipation factors of qSV waves

The sample is the same of the validation experiments but considering 6 periods of 0.012 cm of illite-smectite and 0.003 cm of kerogen (20 % kerogen) and 6 periods of 0.0105 cm of illite-smectite and 0.0045 cm of kerogen (30 % kerogen).$S_g = 10\,\%$ in the illite-smectite and kerogen layers.

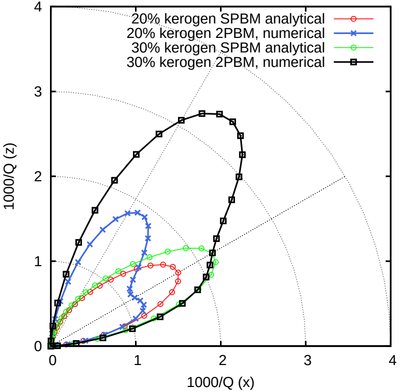

Polar representation of dissipation factors of qSV waves for the FE 2PBM and SPBM models at 50 Hz as a function of kerogen concentration. The medium consists of a sequence of eight (seven) water-gas saturated illite-smectite layers and two (three) oil-gas saturated kerogen layer. Dissipation factors are much higher for the 2PBM model than for the SPBM model. These experiments indicate that the SPBM model is not reliable for predicting attenuation in multiphase saturated porous rocks.

Patchy saturation

We analyze the effect of patchy gas-oil saturation in the kerogen layers for the case of 40 % kerogen concentration. Patchy-saturation patterns produce strong mesoscopic-loss effects at the seismic frequency band.
The first step to generate a patchy fluid distribution is to assign to each sub-domain Ω_j, of the partition of the domain Ω, a pseudo-random number using a generator with uniform distribution. This random field is Fourier transformed to the spatial wave-number domain and its amplitude spectrum is multiplied by the von Karman spectral density:

$$S_d(k_{x_1}, k_{x_3}) = S_0(1 + k^2(CL)^2)^{-(H+N_e/2)} \tag{3}$$

$k = \sqrt{(k_{x_1})^2 + (k_{x_3})^2}$: the radial wave-number,
N_e: the Euclidean dimension,
CL: the correlation length,
H self-similarity coefficient ($0 < H < 1$)
S_0 normalization constant.

Equation (3) corresponds to a fractal process of dimension $D = N_e + 1 - H$ at scales smaller than CL. The resulting fractal spectrum is then transformed back to the spatial domain, obtaining a *micro-heterogeneous* fractal gas saturation model $S_g^{(j)}$.
To generate a binary gas-oil patchy-saturation, choose a threshold value S_g^* and for each Ω_j where $S_g^{(j)} \le S_g^*$ we set $S_g = 1\,\%$, while if $S_g^{(j)} > S_g^*$, $S_g = 30\%$
In the examples, $D = 2.3$ and CL is 1.67 % of the side length of the sample. Residual saturations are $S_{rw} = 10\,\%$ and $S_{rg} = 0$. Saturation in the illite-smectite layers is chosen to be uniform with gas saturation $S_g = 1\,\%$.

Patchy gas-oil distribution in the kerogen layers.

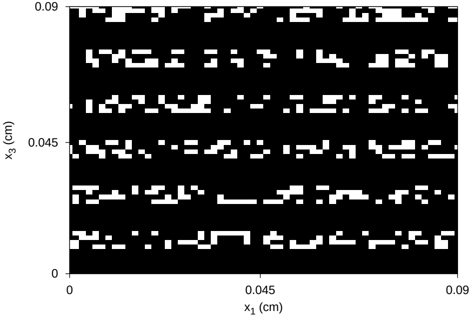

Patchy gas saturation distribution in the kerogen layers. White regions correspond to $S_g = 30\,\%$, black regions correspond to $S_g = 1\,\%$. Overall gas saturation in the kerogen layers is 10 %. The sample is a square of side length 0.09 cm.

Patchy saturation in the kerogen layers. Dissipation factors of qP and qSV waves

Here we analyze the effect of patchy gas-oil saturation in the kerogen layers for the case of 40 % kerogen concentration, both for the SPBM and 2PBM. The results of the SPBM were obtained using FE harmonic experiments and effective single-phase fluids. Energy velocities of qP and qSV waves are not shown since they are very similar for both models.

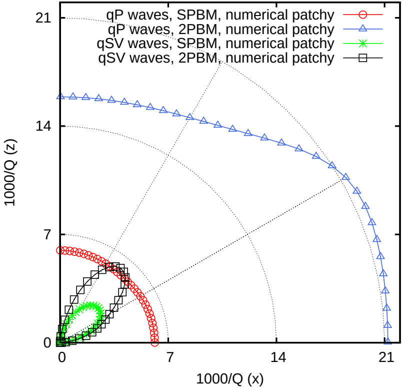

Polar representation of dissipation factors of the qP and qSV waves for the FE 2PBM and FE SPBM models at 50 Hz. Patchy gas-oil distribution in the kerogen layers with overall gas saturation $S_g = 10\%$ with . The medium consists of a sequence of six water-gas saturated illite-smectite layers and four oil-gas saturated kerogen layer (Kerogen concentration is 40 %). $S_g = 1\,\%$ in the illite-smectite layers.

Absolute value of the total fluid pressure distribution at 50 Hz.

The absolute value of the total fluid pressure distribution $\widetilde{\mathcal{T}}$ is defined as $\widetilde{\mathcal{T}} = \mathcal{T}_n + \mathcal{T}_w$.

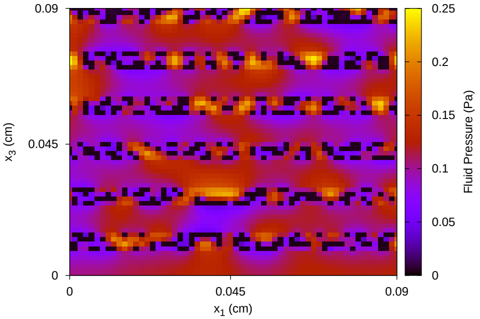

Total pressure gradients are the highest at the gas-oil interfaces. This illustrates the WIFF mechanism.